

Emergence of magnetism in graphene materials and nanostructures

Oleg V. Yazyev*

Department of Physics, University of California, Berkeley, California 94720, USA and
Materials Sciences Division, Lawrence Berkeley National Laboratory, Berkeley, California 94720, USA

(Dated: April 13, 2010)

Magnetic materials and nanostructures based on carbon offer unique opportunities for future technological applications such as spintronics. This article reviews graphene-derived systems in which magnetic correlations emerge as a result of reduced dimensions, disorder and other possible scenarios. In particular, zero-dimensional graphene nanofragments, one-dimensional graphene nanoribbons, and defect-induced magnetism in graphene and graphite are covered. Possible physical mechanisms of the emergence of magnetism in these systems are illustrated with the help of computational examples based on simple model Hamiltonians. In addition, this review covers spin transport properties, proposed designs of graphene-based spintronic devices, magnetic ordering at finite temperatures as well as the most recent experimental achievements.

Contents

I. Introduction	1
II. Brief overview of experimental progress	2
III. Basic computational approaches	3
A. Model Hamiltonians	3
B. Counting rules	5
IV. Finite graphene fragments - a simple illustration	5
V. Zigzag edges and nanoribbons	7
A. Physical mechanism of edge magnetism	7
B. Possible applications in spintronics	9
C. Magnetic ordering at finite temperatures	11
VI. Magnetism in graphene and graphite	12
A. Radiation damage and defects in carbon materials	12
B. Defect-induced magnetism in graphene	13
C. Magnetism in graphite and multilayer graphene	15
VII. Conclusions and perspectives	15
VIII. Acknowledgments	16
References	16

I. INTRODUCTION

Magnetic materials are essential for modern technology. All presently used magnetic materials involve the elements belonging to either the d - or the f -block of the periodic table. For instance, among the periodic table elements only the late transition metals Fe, Co and Ni, are ferromagnets at room temperature. Magnetic ordering in these transition metals originate from the partially filled d -electron bands. However, magnetism is not common for the light p -block elements belonging to the second period of the periodic table, even despite the fact that

carbon is able to form very diverse and complex molecular structures. In principle, such materials may possess a number of attractive properties such as low density, biocompatibility, plasticity, and many others, which stimulates the search for light-element based magnetism (Makarova and Palacio, 2006).

The field of light-element magnetism and, in particular, of carbon-based magnetism is currently gaining increasing importance because of the following two reasons. Firstly, the field of carbon-based magnetism has always been a very controversial area of research which suffered from the poor reproducibility of experimental results. However, the situation seems to be improved over the last few years. Several examples of magnetism in carbon-based materials continue to be reliably reproduced by different research groups. The second driving force is the first isolation of *graphene*, a truly two-dimensional form of carbon which has attracted enormous attention in science and technology (Novoselov *et al.*, 2004). Graphene has a fairly simple honeycomb atomic structure, but rather unique electronic structure with linear band dispersion at the Fermi level (see Fig. 1) which is largely responsible for many novel physical phenomena observed in this material (for review see (Castro Neto *et al.*, 2009; Geim and Novoselov, 2007; Katsnelson, 2007)). Importantly, graphene can also be considered as a unifying concept for understanding a broad class of sp^2 carbon materials which includes polycyclic aromatic molecules, fullerenes, carbon nanotubes, and graphite as well as their further modifications obtained by patterning, chemical treatment, implantation of defects, impurities, etc.

While ideal graphene is nonmagnetic itself, many its derivative materials and nanostructures, both realized in practice and considered theoretically, show various scenarios of magnetism. The magnetic graphene nanostructures are particularly promising for applications in the field of *spintronics*, a very probable future step in the evolution of electronics industry, which promises information storage, processing and communication at faster speeds and lower energy consumption (Awschalom and Flatte, 2007; Chappert *et al.*, 2007; Fert, 2008; Wolf *et al.*,

*Electronic address: yazyev@civet.berkeley.edu

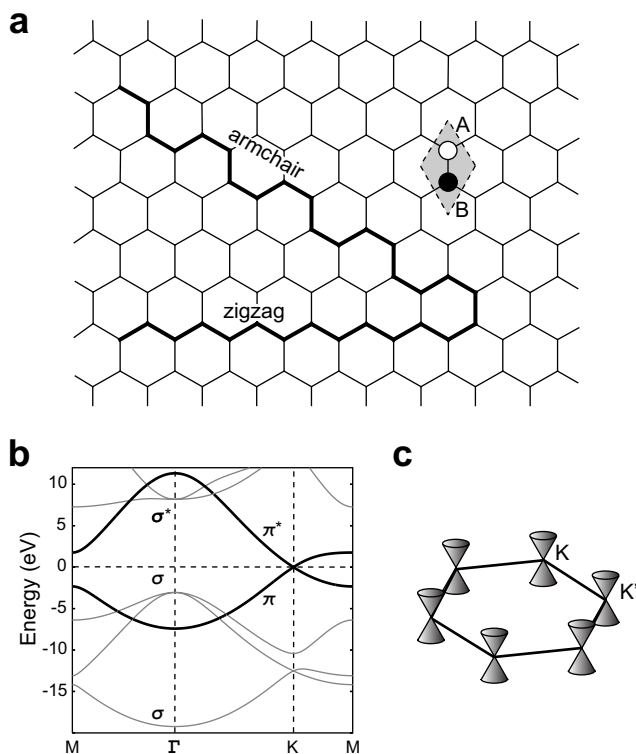


FIG. 1 (a) Two-dimensional crystalline lattice of graphene. The shaded area denotes the unit cell of graphene containing two carbon atoms which belong to the two sublattices of graphene, *A* (empty circle) and *B* (filled circle). The two high-symmetry directions of graphene lattice, armchair and zigzag, are highlighted. (b) Band structure of graphene obtained by means of first-principles calculations. The bands are labeled according to their symmetry. The π -symmetry bands responsible for the low-energy electronic properties of graphene are highlighted. The zero energy corresponds to the Fermi level. (c) The low-energy part of the band structure of graphene involves two inequivalent ‘Dirac cone’ features in the corners (points *K* and *K'*) of the hexagonal Brillouin zone.

2001). While traditional electronics exploits only the charge of electron, spintronics will also make use of its spin degree of freedom. For the field of spintronics graphene can offer a possibility of tuning its spin transport properties by means of various applied stimuli. For instance, it was suggested that half-metallicity of zigzag graphene nanoribbons can be triggered by external electric fields (Son *et al.*, 2006b). If realized in practice, this would allow for efficient electric control of spin transport, a very desirable effect which is hard to achieve using other materials. In addition, materials based *sp*-elements are expected to have high magnitudes of the spin-wave stiffness (Edwards and Katsnelson, 2006) and, thus, nanostructures made of these elements would possess higher Curie temperatures or spin correlation lengths (Yazyev and Katsnelson, 2008). Materials based on light elements also display weak spin-orbit and hyperfine couplings which are the main channels of relaxation

and decoherence of electron spins (Fischer *et al.*, 2009; Trauzettel *et al.*, 2007; Yazyev, 2008a). This property makes carbon nanomaterials promising for transport of spin-polarized currents and for spin-based quantum information processing.

This review provides a brief introduction into the current state of the field of magnetic materials and nanostructures based on graphene. The possible scenarios for the onset of magnetism in graphene nanostructures are illustrated by means of a simple theoretical model based on the mean-field Hubbard Hamiltonian. The next section briefly reviews the landmark experimental reports in the field. Then follows the introduction of the theoretical model and its specific consequences for describing the electronic structure and magnetic properties of graphene-based materials. The main part of this article applies the theoretical model described and reviews both theoretical and experimental published works on magnetic graphene systems classified according to their dimensionality: (1) finite graphene nanofragments, (2) one-dimensional graphene edges and graphene nanoribbons, and (3) two-dimensional graphene and graphite with magnetism induced by the presence of point defects. Of these three classes, magnetic graphene edges and nanoribbons will be covered in more detail since these one-dimensional objects continue to receive special attention in the scientific community. Future perspectives of the field are outlined in the last section.

II. BRIEF OVERVIEW OF EXPERIMENTAL PROGRESS

The first reproducible experimental reports of magnetism in *p*-block compounds were published in 1991 when magnetic ordering was observed in crystalline *p*-nitrophenyl nitronyl nitroxide (*p*-NPNN) (Takahashi *et al.*, 1991; Tamura *et al.*, 1991) and in a charge transfer complex of C_{60}

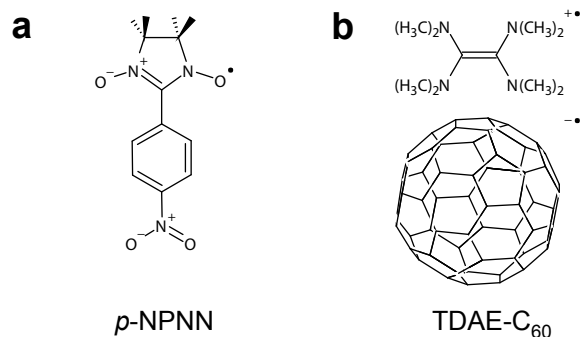


FIG. 2 Chemical structures of (a) *p*-NPNN and (b) the TDAE- C_{60} charge transfer complex. Molecular crystals of these organic compounds exhibit ferromagnetic ordering with Curie temperatures of 0.6 K and 16 K, respectively. Each molecular radical unit bears a single uncompensated electron spin. In chemical notation the presence of unpaired electron is usually denoted by a thick dot.

and tetrakis(dimethylamino)ethylene (TDAE) (Allemand *et al.*, 1991). Molecular structures of these organic materials made of light elements only (C, H, N and O) are shown in Figure 2. In their molecular crystals the uncompensated electron spins are localized on weakly coupled molecular units. Because of the weak coupling between electron spins, the long-range magnetic order is realized only at low temperatures. The two organic materials mentioned above, *p*-NPN and TDAE-C₆₀, are characterized by Curie temperatures of 0.6 K and 16 K, respectively. Since 1991 a large number of other organic magnetic materials have been examined. In all cases the temperatures below which long-range magnetic order is established (Curie temperatures, T_C , and Néel temperatures, T_N , in the case of ferromagnetic and antiferromagnetic orderings, respectively) were much lower than room temperature, which renders such materials useless for practical applications.

The next milestone experiment was reported ten years later when ferromagnetism with $T_C \approx 500$ K was observed in rhombohedral C₆₀ under high pressure (Makarova *et al.*, 2001). This observation, however, demonstrates very well the controversial character of the field. Five years later several authors retracted the original publication since the measured content of magnetic impurities was shown to be close to the amount needed to explain the observed magnetization of the samples (Makarova *et al.*, 2006). In addition, the measured T_C was found to be very similar to the one of cementite Fe₃C. The question of possible high-temperature magnetic ordering in C₆₀-based materials remains open.

Two years later room-temperature ferromagnetism was observed in highly oriented pyrolytic graphite (HOPG) irradiated with high-energy (2.25 MeV) protons (Esquinazi *et al.*, 2003). Figure 3 shows the magnetization loop for a proton-irradiated sample compared

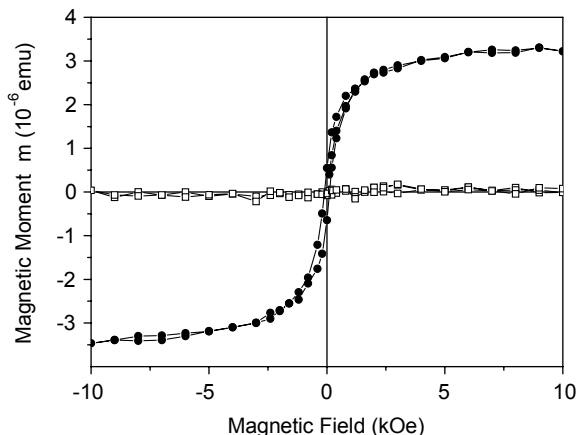


FIG. 3 Magnetic moment of proton irradiated (filled circles) and untreated (empty squares) graphite as a function applied magnetic field as measured by Esquinazi *et al.* at $T = 300$ K. The weak hysteresis loop can be recognized. Reprinted from (Esquinazi *et al.*, 2003). Copyright 2003 by the American Physical Society.

to untreated HOPG. Further experimental investigations revealed that the magnetic order in proton-bombarded graphite has two-dimensional, that is, graphene-like character (Barzola-Quiquia *et al.*, 2007) and originates from the carbon π -electron system rather than from possible *d*-element impurities (Ohldag *et al.*, 2007). Interestingly, it was shown that the chemical nature of the high-energy particles plays a crucial role in producing magnetic ordering. While proton irradiation leads to the onset of ferromagnetism in irradiated samples, both helium (Esquinazi *et al.*, 2003) and iron (Barzola-Quiquia *et al.*, 2008) ions show no clear effect. On the other hand, the implantation of carbon ions was also reported to induce ferromagnetism in HOPG (Xia *et al.*, 2008).

A number of reports have also pointed out that even untreated graphite exhibit ferromagnetism (Esquinazi *et al.*, 2002; Kopelevich *et al.*, 2000). Very recently, by using a combination of scanning probe techniques and magnetization measurements, Červenka and co-authors have shown that the intrinsic ferromagnetism of graphite is related to the presence of grain boundaries which can be considered as 2D periodic networks of point defects (Červenka *et al.*, 2009). Room-temperature magnetic hysteresis has also been reported for graphene samples produced in bulk quantities from graphite using the chemical approaches (Matte *et al.*, 2009; Wang *et al.*, 2009b).

III. BASIC COMPUTATIONAL APPROACHES

A. Model Hamiltonians

The vast majority of computational studies of magnetic carbon nanostructures are currently performed using first-principles electronic structure methods based on density functional theory (DFT). This approach is now implemented in a large number of public computer codes and well described in a variety of graduate-level textbooks (for instance, see (Koch and Holthausen, 2002; Martin, 2004; Marx and Hutter, 2009)). For pedagogical purposes, a simpler approach based on model Hamiltonians will be adopted in this review article. Moreover, it will be demonstrated below that such simplified models very often allow deeper understanding of the results obtained.

A simple model which is widely used for studying magnetic effects in sp^2 carbon materials is the one-orbital mean-field Hubbard model. This model considers only the π -symmetry electronic states which are formed by the unhybridized p_z atomic orbitals of sp^2 carbon atoms. As shown in Figure 1(b) the low-energy electronic states have π -symmetry and thus play the dominant role in the properties of graphene systems. The Hubbard model Hamiltonian can be partitioned into two parts,

$$\mathcal{H} = \mathcal{H}_0 + \mathcal{H}'. \quad (1)$$

The first term is the nearest-neighbor tight-binding

Hamiltonian

$$\mathcal{H}_0 = -t \sum_{\langle i,j \rangle, \sigma} [c_{i\sigma}^\dagger c_{j\sigma} + \text{h.c.}], \quad (2)$$

in which the operators $c_{i\sigma}$ and $c_{i\sigma}^\dagger$ annihilate and create an electron with spin σ at site i , respectively. The notation $\langle \cdot, \cdot \rangle$ stands for the pairs of nearest-neighbor atoms; ‘h.c.’ is the Hermitian conjugate counterpart. The well established hopping integral $t \approx 2.7$ eV defines the energy scale of the Hamiltonian. This physical model is equivalent to the Hückel method familiar to chemists. From the computational point of view, the Hamiltonian matrix is determined solely by the atomic structure: the off-diagonal matrix elements (i, j) and (j, i) are set to $-t$ when atoms i and j are covalently bonded, and to 0 otherwise. In a neutral graphene system each sp^2 carbon atom contributes one p_z orbital and one π electron. The π -electron system is thus called half-filled. The spectrum of the eigenvalues of tight-binding Hamiltonian matrix exhibit electron-hole symmetry, *i.e.* it is symmetric with respect to zero energy. In other words, in a neutral graphene system for each eigenvalue $\epsilon < 0$ corresponding to an occupied (bonding) state, there is an unoccupied (anti-bonding) state with $\epsilon^* = -\epsilon$. The states with $\epsilon = 0$ are called zero-energy states (also referred to as non-bonding or midgap states).

The nearest-neighbor tight-binding model has proved to describe accurately the electronic structure of graphene, carbon nanotubes and other non-magnetic sp^2 carbon materials. However, electron-electron interactions have to be introduced in some form in order to describe the onset of magnetism. Within the Hubbard model these interactions are introduced through the repulsive on-site Coulomb interaction

$$\mathcal{H}' = U \sum_i n_{i\uparrow} n_{i\downarrow}, \quad (3)$$

where $n_{i\sigma} = c_{i\sigma}^\dagger c_{i\sigma}$ is the spin-resolved electron density at site i ; the parameter $U > 0$ defines the magnitude of the on-site Coulomb repulsion. This model considers only the short-range Coulomb repulsion, that is, two electrons interact only if they occupy the p_z atomic orbital of the same atom. Despite its apparent simplicity, this term is no longer trivial from the computational point of view. The mean-field approximation

$$\mathcal{H}'_{\text{mf}} = U \sum_i (n_{i\uparrow} \langle n_{i\downarrow} \rangle + \langle n_{i\uparrow} \rangle n_{i\downarrow} - \langle n_{i\uparrow} \rangle \langle n_{i\downarrow} \rangle), \quad (4)$$

allows us to overcome this difficulty. Here, a spin-up electron at site i interacts with the average spin-down electron population $\langle n_{i\downarrow} \rangle$ at the same site, and vice versa. This mean-field model represents a variation of the unrestricted Hartree-Fock method (Szabo and Ostlund, 1982). From the computational point of view, the electron-electron interaction term affects only the diagonal elements of the Hamiltonian matrix. The diagonal elements of the spin-up and spin-down blocks now

depend on the unknown $\langle n_{i\downarrow} \rangle$ and $\langle n_{i\uparrow} \rangle$, respectively. The problem can be solved self-consistently starting from some initial values of $\langle n_{i\sigma} \rangle$ which can be chosen randomly. However, one has to keep in mind that in certain cases the broken-symmetry (antiferromagnetic) solutions can be obtained only if the initial guess breaks the spin-spatial symmetry (Yazyev *et al.*, 2008). The process of (1) calculation of the matrix elements of the Hamiltonian matrix, (2) its diagonalization and (3) the computation of updated spin densities is then repeated iteratively until all values of $\langle n_{i\sigma} \rangle$ are converged. The final self-consistent solution provides the spin densities

$$M_i = \frac{\langle n_{i\uparrow} \rangle - \langle n_{i\downarrow} \rangle}{2}, \quad (5)$$

at each atom i and the total spin of the system $S = \sum_i M_i$. For a given graphene structure both local and total spins (magnetic moments) depend exclusively on the dimensionless parameter U/t .

After the model has been introduced, the following three critical questions can be asked. (1) Is the one-orbital approximation accurate enough compared to the methods considering all electrons? (2) Which value of the empirical parameter U/t should be used? (3) Is the mean-field approximation justified for graphene based systems?

(1) It has been shown that the results of mean-field Hubbard model calculations correspond closely to the ones obtained using first-principles methods if the parameter U/t is chosen appropriately (Fernández-Rossier and Palacios, 2007; Gunlycke *et al.*, 2007; Pisani *et al.*, 2007). The first-principles methods either treat all electrons on equal footing or disregard the localized atomic core states which are not important in most cases. One notable exception is the calculation of hyperfine interactions. In this case the spin polarization of the 1s atomic core states of carbon atoms has significant contribution to the Fermi contact hyperfine couplings (Yazyev, 2008a; Yazyev *et al.*, 2005). Otherwise, the results of DFT calculations performed using a generalized-gradient-approximation family exchange-correlation functional are best reproduced when $U/t \approx 1.3$. The results of the local-spin-density approximation calculations are best fitted using $U/t \approx 0.9$ (Pisani *et al.*, 2007).

(2) Ideally, the empirical parameter U/t must be estimated using experimental knowledge. Unfortunately, there are no direct experiments performed on magnetic graphene systems which would allow to estimate U/t . Magnetic resonance studies of neutral soliton states in *trans*-polyacetylene, a one-dimensional sp^2 carbon polymer which can be viewed as a minimum-width zigzag graphene nanoribbon, give the range of values $U \sim 3.0$ – 3.5 eV (Kuroda and Shirakawa, 1987; Thomann *et al.*, 1985). This interval corresponds to $U/t \sim 1.1$ – 1.3 which also makes us confident in the results of the generalized-gradient-approximation DFT calculations. Increasing U/t leads to the enhancement

of magnetic moments. The range of meaningful magnitudes is limited by $U/t \approx 2.23$ above which the ideal graphene undergoes a Mott-Hubbard transition into an antiferromagnetically ordered insulating state (Sorella and Tosatti, 1992). In the computational examples considered below a value of $U/t = 1.2$ will be used.

(3) This question is the most difficult to answer. A comparison of the mean-field results with the ones obtained using exact diagonalization and quantum Monte Carlo simulations illustrates the validity of this approximation for the relevant values of U/t (Feldner *et al.*, 2009). Magnetic graphene materials and nanostructures need not be considered as strongly correlated systems.

B. Counting rules

There are two important consequences coming from the model Hamiltonians we have introduced. The honeycomb lattice of graphene is a *bipartite* lattice. That is, it can be partitioned into two mutually interconnected sublattices A and B (see Fig. 1(a)). Each atom belonging to sublattice A is connected to the atoms in sublattice B only, and vice versa. Moreover, the graphene systems whose faces are hexagons are called benzenoid (or honeycomb) systems. Carbon atoms in such systems have either three or two nearest neighbors. The class of benzenoid systems is a subclass of bipartite systems.

The spectrum of the tight-binding Hamiltonian of a honeycomb system can be analyzed using a mathematically rigorous approach of the benzenoid graph theory (Fajtlowicz *et al.*, 2005). An important result for us is that this theory is able to predict the number of zero-energy states of the nearest-neighbor tight-binding Hamiltonian in a ‘counting rule’ fashion. The number of such states is equal to the graph’s nullity

$$\eta = 2\alpha - N, \quad (6)$$

where N is the total number of sites and α is the maximum possible number of non-adjacent sites, *i.e.* the sites which are not the nearest neighbors to each other. The onset of magnetism in the system is determined by the so-called Stoner criterion which refers to the competition of the exchange energy gain and the kinetic-energy penalty associated with the spin-polarization of the system (Mohn, 2003). The gain in exchange energy is due to the exchange splitting of the electronic states subjected to spin-polarization (Palacios *et al.*, 2008)

$$\Delta_S = \epsilon_{\uparrow} - \epsilon_{\downarrow} = \frac{U}{2} \sum_i n_i^2, \quad (7)$$

where $\sum_i n_i^2$ is the inverse participation ratio, a measure of the degree of localization of the corresponding electronic state. The kinetic-energy penalty is proportional to the energy of this state. Thus, the zero-energy states undergo spin-polarization at any $U > 0$ irrespective of their degree of localization. One can view spin-polarization as one of the mechanisms for escaping an

instability associated with the presence of low-energy electrons in the system. Other mechanisms, such as the Peierls distortion, were shown to be inefficient in the case of graphene nanostructures (Pisani *et al.*, 2007).

Although the benzenoid graph theory is able to predict the occurrence of zero-energy states, it is not clear how the electron spins align in these states. The complementary knowledge is supplied by Lieb’s theorem (Lieb, 1989) which determines the total spin of a bipartite system described by the Hubbard model. This theorem states that in the case of repulsive electron-electron interactions ($U > 0$), a bipartite system at half-filling has the ground state characterized by the total spin

$$S = \frac{1}{2}|N_A - N_B|, \quad (8)$$

where N_A and N_B are the numbers of sites in sublattices A and B , respectively. The ground state is unique and the theorem holds in all dimensions without the necessity of a periodic lattice structure. Importantly, the two counting rules are linked by the following relation, $\eta \geq |N_A - N_B|$.

In the following section, the application of these two simple counting rules will be demonstrated on small graphene fragments and compared to the results of numerical calculations.

IV. FINITE GRAPHENE FRAGMENTS - A SIMPLE ILLUSTRATION

Let us first try to understand the origin of magnetism in finite graphene fragments (also referred to as nanoflakes, nanoislands or nanodisks) as a function of their shape and size. Three simple examples of nanometer sized graphene fragments are shown in Figure 4. From the point of view of single-orbital physical models, only the connectivity of the π -electron conjugation network is important. Such π -systems may constitute only small parts of more complex molecules or bulk materials. In simplest case, the π -electron networks shown in Figure 4 can be realized in the corresponding all-benzenoid polycyclic aromatic hydrocarbon (PAH) molecules with the edges of the fragments being passivated by hydrogen atoms. Each carbon atom at the edge of the fragment is bonded to one hydrogen atom such that all carbon atoms are sp^2 -hybridized. Current progress in synthesizing such molecules and understanding their properties has recently been reviewed (Wu *et al.*, 2007).

The hexagonal graphene fragment shown in Figure 4(a) is thus equivalent to the *coronene* molecule. For this fragment, the number of sites belonging to the two sublattices is equal, $N_A = N_B = 12$. The number of non-adjacent sites is maximized when all atoms belonging to either of the two sublattices are selected, *i.e.* $\alpha = 12$. Thus, both the number of zero-energy states η and the total spin S are zero. The tight-binding model predicts a wide band gap of $1.08t \approx 3.0$ eV for this graphene

molecule. As expected, the mean-field Hubbard model solution for this fragment does not reveal any magnetism.

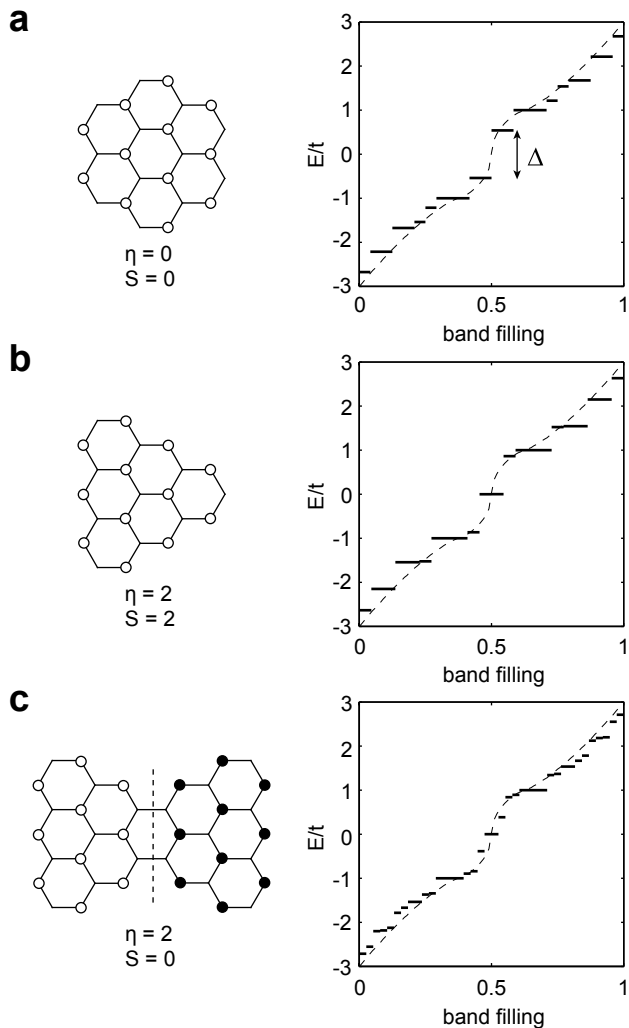


FIG. 4 Atomic structures and tight-binding energy spectra of three graphene fragments: (a) coronene, (b) triangulane, and (c) a bowtie-shaped fragment (“Clar’s goblet”). Non-adjacent sites are labeled by circles. Empty and filled circles correspond to sublattice A and sublattice B , correspondingly. Tight-binding energies are plotted as a function of band filling. Dashed line corresponds to the energy spectrum of ideal graphene.

The second graphene fragment shown in Figure 4(b) has triangular shape. It is not surprising that the corresponding hypothetical PAH molecule is called *triangulane*. Unlike coronene, the two sublattices of this triangular fragment are no longer equivalent: $N_A = 12$ and $N_B = 10$. The unique choice maximizing the number of non-adjacent sites is achieved by selecting the atoms belonging to the dominant sublattice A , *i.e.* $\alpha = N_A = 12$. Thus, the benzenoid graph theory predicts the presence of two zero-energy states on sublattice A . Lieb’s theorem predicts the $S = 1$ (spin-triplet) ground state or, equivalently, a magnetic moment of $2 \mu_B$ per molecule. The two low-energy electrons populate a pair of zero-energy

states according to Hund’s rule, that is, their spins are oriented parallel to each other. The mean-field Hubbard model results for this system at half-filling are shown in Figure 5(a). One can see that spin-polarization lifts the degeneracy of the zero-energy electronic states and opens an energy gap $\Delta_S = 0.30t \approx 0.8$ eV. The system is stabilized by spin-polarization. Most of the spin-up electron density localized on the atoms in sublattice A (see Fig. 5(a)) originates from the two electrons populating the non-bonding states. However, one can notice an appreciable amount of spin-down density on the atoms in sublattice B which is compensated by an equivalent contribution of the spin-up density in sublattice A . The occurrence of the induced magnetic moments is a manifestation of the spin-polarization effect which is related to the exchange interaction of the fully populated states with the two unpaired electrons.

The third bowtie-shaped graphene molecule shown in Figure 4(c) is composed of two triangulane fragments sharing one hexagon. For this system Lieb’s theorem predicts the spin-singlet ground state ($N_A = N_B = 19$). However, the choice of the set of atoms which maxi-

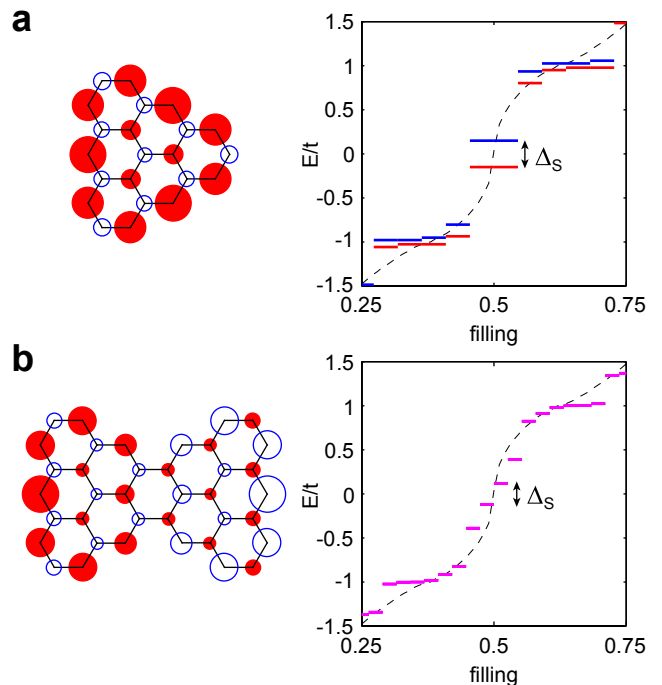


FIG. 5 Local magnetic moments and spin-resolved energy levels obtained through the mean-field Hubbard model calculations for (a) triangulane and (b) the bowtie-shaped graphene fragment ($U/t = 1.2$). Area of each circle is proportional to the magnitude of the local magnetic moment at each atom. Filled (red) and empty (blue) circles correspond to spin-up and spin-down densities. Energy levels energies are plotted as a function of band filling. Dashed line corresponds to the energy spectrum of ideal graphene. Red and blue levels correspond to spin-up and spin-down channels, respectively. In the case of bowtie fragment the energies in the two channels are identical (shown in magenta).

mizes the number non-adjacent sites is less evident in this case. Figure 4(c) shows such a selection ($\alpha = 20$) which involves the atoms belonging to both sublattice *A* and sublattice *B* in the left and right parts of the structure. These atoms are marked differently in the figure. Hence, there are $\eta = 2 \times 20 - 38 = 2$ zero-energy states as confirmed by the tight-binding calculation. The zero-energy states are spatially segregated in the two triangular parts of the molecule (Wang *et al.*, 2009a). To satisfy the spin-singlet ground state, the two zero-energy states have to be populated by two electrons with oppositely oriented spins. In other words, the ground electronic configuration breaks spin-spatial symmetry and exhibits antiferromagnetic ordering. This result can be verified by mean-field Hubbard model calculations as shown in Figure 5(b). It can be argued that this example violates Hund's rule. However, one has to keep in mind that each of the two non-bonding states is localized within one of the graphene sublattices. That is, there are two electronic sub-bands, each populated by electrons according to Hund's rule. The coupling between the electron spins in these two sub-bands is antiferromagnetic due to the superexchange mechanism (Anderson, 1950; Kramers, 1934).

The two counting rules can be applied to larger graphene fragments. It was shown that the total spin of triangular fragments with edges cut along the zigzag direction scales linearly with fragment size (Ezawa, 2007; Fernández-Rossier and Palacios, 2007; Wang *et al.*, 2008a) as illustrated in Figure 6. The average magnetic moment per carbon atom thus decays with increasing the system size. The evolution of magnetic properties with increasing size for hexagonal fragments with edges cut along the same zigzag direction is less trivial. It has been shown theoretically that above some critical size the system undergoes a transition into a broken-symmetry antiferromagnetic state (Fernández-Rossier and Palacios, 2007). The critical size itself depends strongly on the value of U/t . However, it is easier to explain the origin of this behavior in large systems from the standpoint of edge magnetism, which will be explained in the next section.

Finally, a few words have to be said about the possibility of realizing in practice the magnetic graphene fragments we have discussed. It is expected that such magnetic systems are more reactive than the non-magnetic polyaromatic molecules. Although triangulane itself has

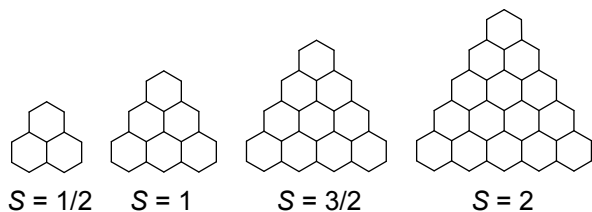


FIG. 6 Evolution of the total spin of triangular graphene fragments with size.

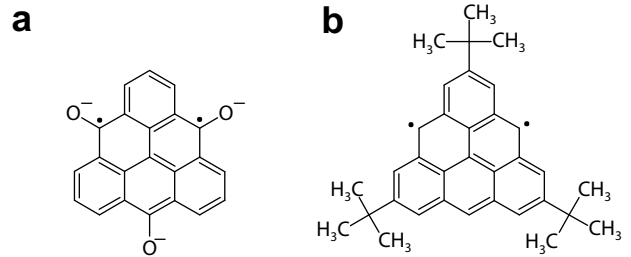


FIG. 7 Chemical derivatives of triangulane synthesized by (Allinson *et al.*, 1995) and (Inoue *et al.*, 2001). Their spin-triplet ground state has been verified by means of electron spin resonance measurements.

never been isolated, successful synthesis of its chemical derivatives shown in Figure 7 has been reported (Allinson *et al.*, 1995; Inoue *et al.*, 2001). The spin-triplet ground state of these chemical compounds was verified by the electron spin resonance measurements. In principle, this example can be considered as an indirect proof of edge magnetism in graphene systems, at least in finite fragments produced by means of the chemical bottom-up approach. The synthesized triangulane derivatives are reactive molecules, but nevertheless can be handled in common organic solvents and stored for many months at room temperature provided the solution is isolated from atmospheric oxygen (Allinson *et al.*, 1995). Larger magnetic triangular molecules have not been synthesized so far. The PAH molecule corresponding to the considered bowtie fragment was hypothesized by Eric Clar and named “Clar’s goblet” after him (Clar, 1972). Attempts to synthesize this molecule have failed (Clar and Mackay, 1972).

The examples shown above illustrate how three different magnetic scenarios can be realized in very simple finite graphene systems. These examples also provide a way for designing nanostructures with predefined magnetic interactions, a highly useful tool for developing novel spintronic devices. The value of this approach has already been demonstrated by the proposal of reconfigurable spintronic logic gates exploiting the strong antiferromagnetic couplings in the bowtie-shaped graphene fragments (Wang *et al.*, 2009a). Several devices for controlling spin-currents based on triangular graphene fragments have also been described recently (Ezawa, 2009b). A number of other intriguing properties predicted for zero-dimensional graphene fragments are potentially interesting from both fundamental and applied points of view (Akola *et al.*, 2008; Ezawa, 2008, 2009a).

V. ZIGZAG EDGES AND NANORIBBONS

A. Physical mechanism of edge magnetism

As one moves on towards larger graphene fragments or infinite systems, the application of counting rules be-

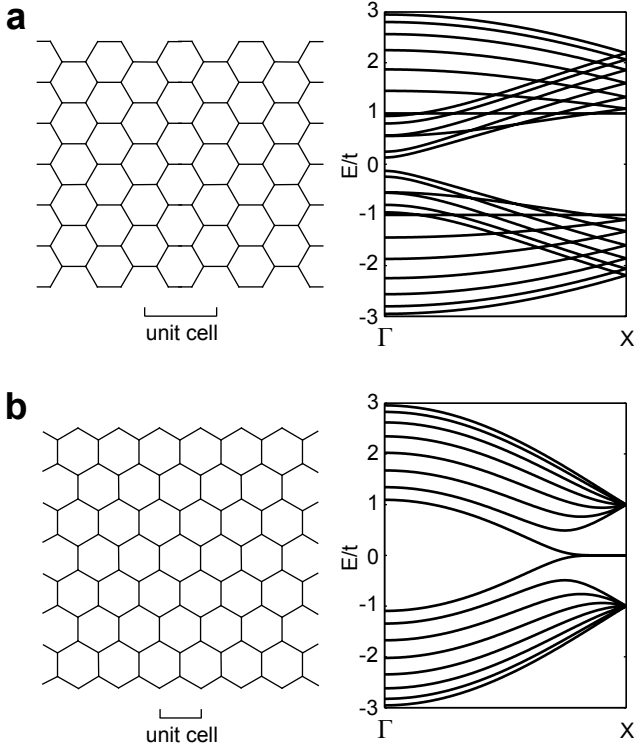


FIG. 8 Atomic structures and tight-binding band structures of (a) armchair and (b) zigzag graphene nanoribbons. Unit cells of the graphene nanoribbons are shown.

comes impractical. An alternative approach considers the effects of edges of graphene nanostructures which can be conveniently modeled using one-dimensional periodic strips of graphene. Such models are commonly referred to as *graphene nanoribbons*. There are two high-symmetry crystallographic directions in graphene, *armchair* and *zigzag*, as shown in Figure 1(a). Cutting graphene nanoribbons along these directions produces armchair and zigzag nanoribbons, respectively (Fig. 8).

The band structures of armchair and zigzag nanoribbons are remarkably different. Figure 8(a) shows the tight-binding band structure of a ~ 1.5 nm wide armchair nanoribbon. For this particular armchair graphene nanoribbon, introducing a pair of parallel armchair edges opens a gap of $0.26t$. The nearest-neighbor tight-binding model predicts either metallic or semiconducting behavior for armchair nanoribbons (Barone *et al.*, 2006; Brey *et al.*, 2007; Ezawa, 2006; Nakada *et al.*, 1996; Peres *et al.*, 2006; Son *et al.*, 2006a), and the two situations alternate as the nanoribbon's width increases. The band gap of semiconducting graphene nanoribbons decreases with increasing width. In the case of metallic nanoribbons two bands cross the Fermi level at the Γ point. No magnetic ordering is predicted in this case.

Within the same model all zigzag graphene nanoribbons are metallic and feature a flat band extending over one-third of the one-dimensional Brillouin zone at $k \in (2\pi/3a; \pi/a)$ ($a = 0.25$ nm is the unit cell of the

zigzag edge) as shown in Figure 8(b). Strictly speaking, the flat band does not correspond to zero-energy states, but rather to the states with energies the approach zero with increasing nanoribbon width. The low-energy states are localized at the edge and decay quickly in the bulk.

High density of low-energy electronic states suggests a possibility of magnetic ordering. Indeed, the mean-field Hubbard model solution for this system reveals magnetic moments localized at the edges as shown in Figure 9(a). The localized magnetic moments display ferromagnetic ordering along the zigzag edge while the mutual orientation of the magnetic moments localized at the opposite edges is antiparallel (Fernández-Rossier, 2008; Fujita *et al.*, 1996; Son *et al.*, 2006b). Thus, the net magnetic moment of a zigzag nanoribbon is zero in agreement with Lieb's theorem ($N_A = N_B$). The band structure corresponding to the mean-field Hubbard model solution is compared to the tight-binding band structure in Figure 9(b). The introduced electron-electron interactions open a band gap across the whole flat-band segment

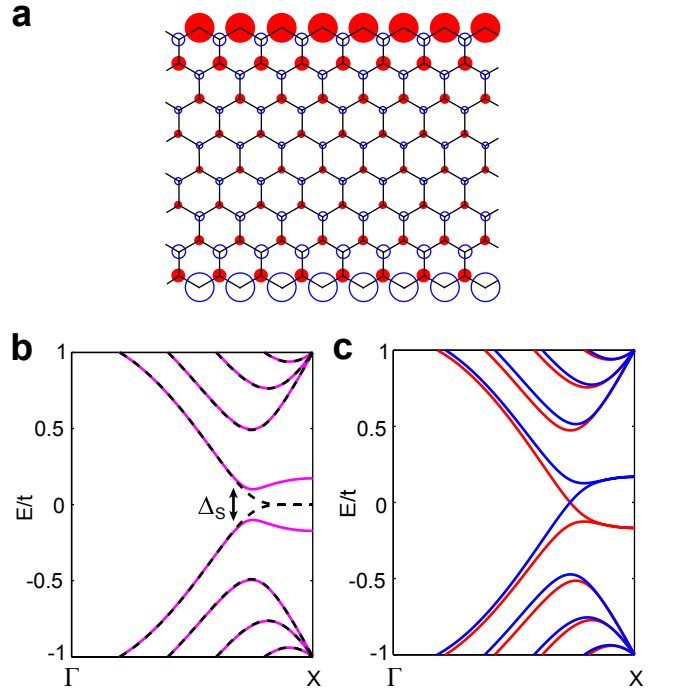


FIG. 9 (a) Local magnetic moments in a zigzag graphene nanoribbon calculated using the mean-field Hubbard model ($U/t = 1.2$). Area of each circle is proportional to the magnitude of the local magnetic moment at each atom. Filled (red) and empty (blue) circles correspond to spin-up and spin-down densities, respectively. (b) Mean-field Hubbard-model band structure (solid magenta lines) compared to the tight-binding band structure (dashed lines) for the solution shown in panel (a). The band structures for spin-up and spin-down electrons are equivalent. (c) Mean-field Hubbard-model band structure for the same graphene nanoribbon with the ferromagnetic mutual orientation of the edge spins. The band structures for the majority-spin electrons and the minority-spin electrons are shown as red and blue lines, respectively.

turning the system into a semiconductor ($\Delta_S = 0.20t$ at $U/t = 1.2$). The spin-polarization almost does not affect the electronic states at higher energies. The band structures for the two spin channels are equivalent, but spin-spatial symmetry is broken.

The coupling between the magnetic edges can be ascribed to the superexchange mechanism as in the case of bowtie graphene fragment considered in the previous section. The magnitude of the antiferromagnetic coupling shows a w^{-2} dependence as a function of nanoribbon width w (Jung *et al.*, 2009). The interedge magnetic coupling strength of ~ 25 meV has been calculated from first principles for a ~ 1.5 nm wide nanoribbon (Pisani *et al.*, 2007). Unlike the antiferromagnetic ground state, a zigzag graphene nanoribbon with ferromagnetic interedge orientation is a metal with two bands crossing the Fermi level at $k \approx 2\pi/3a$ (Fig. 9(c)). The possibility of switching between the two states was exploited in a proposal of a graphene-based magnetic sensor (Muñoz-Rojas *et al.*, 2009) described in the next section. The coupling between the magnetic moments localized at the edges can be controlled by means of either electron or hole doping of the nanoribbons (Jung and MacDonald, 2009; Sawada *et al.*, 2009). High doping levels eventually suppress magnetism since the flat band shifts away from

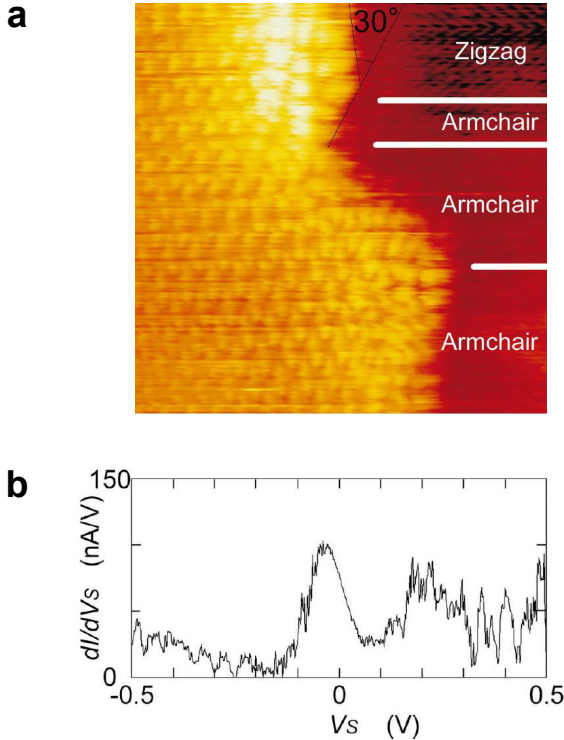


FIG. 10 (a) An atomically resolved STM image showing the presence of both armchair and zigzag graphene edges. (b) Typical STS curve measured at a zigzag edge reveals the peak related to zero-energy states. Reproduced from (Kobayashi *et al.*, 2005). Copyright 2005 by the American Physical Society.

the Fermi level, thus eliminating the electronic instability associated with the presence of low-energy electrons (Jung and MacDonald, 2009).

It is worth mentioning that at the time this review was written, no direct proof of edge magnetism in graphene has been reported. However, the presence of localized low-energy states at zigzag edges of graphene has been verified by means of scanning tunneling microscopy (Kobayashi *et al.*, 2006, 2005).

B. Possible applications in spintronics

It has been realized that the intriguing magnetic properties of graphene nanostructures may find applications in spintronics. The pioneering idea was introduced by Son, Cohen and Louie, who have predicted that external electric fields induce *half-metallicity* in zigzag graphene nanoribbons (Son *et al.*, 2006b). The half-metallicity refers to the coexistence of a metallic state for electrons with one spin orientation and an insulating state for electrons with the opposite spin orientation. An electric field is applied across the nanoribbon as shown in Figure 11(a). At zero field the system is characterized by the energy gap Δ_S for the spin-polarized states localized at both edges (Fig. 11(b)). An applied electric field breaks the symmetry and closes the gap for one of the spin directions selectively (Fig. 11(c)). The critical field required

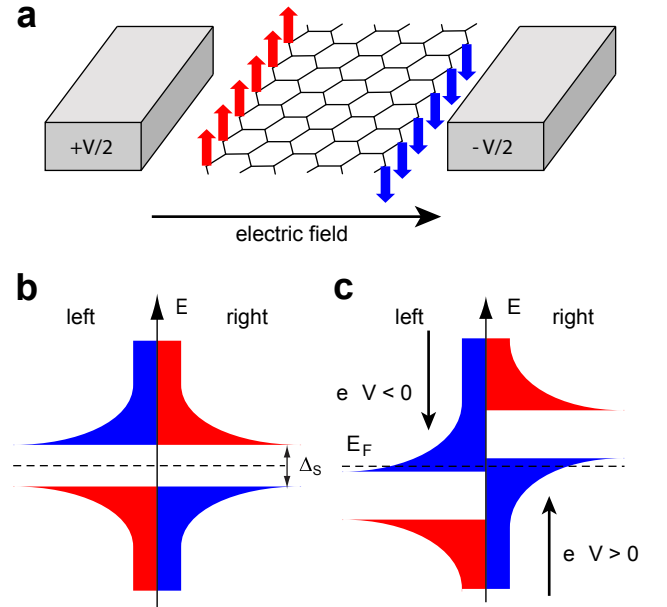


FIG. 11 Scheme of electric-field-induced half-metallicity in zigzag graphene nanoribbons. (a) Electric field is applied across the nanoribbon, from left edge (spin-up, red arrows) to right edge (spin-down, blue arrows). (b) Schematic representation of the spin-resolved local density of states for the opposite edges at zero applied field. (c) Applied electric field closes the band gap at the Fermi level E_F for spin-down electrons selectively.

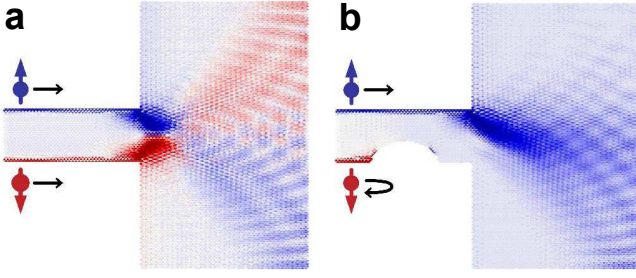


FIG. 12 Spin injection from (a) an ideal zigzag graphene nanoribbon and (b) a nanoribbon with a defective bottom edge into *n*-doped graphene (Wimmer *et al.*, 2008). Nonequilibrium densities for spin-up and spin down-electrons are shown in blue and red, respectively. Copyright 2008 by the American Physical Society.

for inducing the half-metallicity is $3.0/w$ Volts, where w is the nanoribbon width in Å. The direction of the applied electric field defines the spin channel with metallic conductivity. If realized in practice, this simple device would offer efficient electrical control of spin transport – a highly desirable component for spintronics.

In addition to the device described, several other approaches for controlling the spin transport in graphene nanostructures have been proposed. One of them exploits disorder for achieving the goal; an example from (Wimmer *et al.*, 2008) is shown in Figure 12. Electric current flowing along the edges of zigzag nanoribbon injects spin-polarized electrons into a graphene reservoir (Fig. 12(a)). However, the net spin-polarization of the current is zero due to the antiferromagnetic coupling between the two equivalent edges. Then, an extended defect is introduced into one of the edges as shown in Figure 12(b). The defect both quenches magnetic moments and scatters the carriers at the rough edge. However, conduction at the opposite edge remains unaffected, thus allowing for injecting a current with a net spin polarization. Other proposals based on defect and impurity engineering of spin transport in graphene nanoribbons have been reported (Cantele *et al.*, 2009; Lakshmi *et al.*, 2009; Park *et al.*, 2009; Rocha *et al.*, 2009).

Magnetic graphene nanostructures were also proposed as components of magnetoresistive junctions. Such devices are currently used as magnetic field sensors, *e.g.* in the read heads of hard disk drives. Typical magnetoresistive junctions involve ferromagnetic metal layers separated by a nonmagnetic spacer layers, *e.g.* Co layers separated by a non-magnetic Cu layer, or bcc Fe layers separated by a few-nanometers thick layer of crystalline MgO. A crucial characteristic of such spintronic devices is their magnetoresistance ratio (MR) which shows the change in electric resistance as a function of the relative orientation of the magnetization of two ferromagnetic layers (Heiliger *et al.*, 2006). This quantity can be defined as

$$\text{MR} = \frac{R^{\text{AP}} - R^{\text{P}}}{\min(R^{\text{P}}, R^{\text{AP}})} \times 100\%, \quad (9)$$

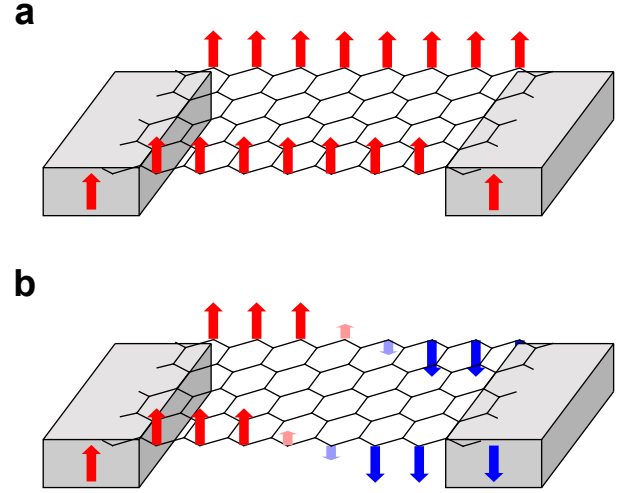


FIG. 13 Scheme of magnetoresistive device based on zigzag graphene nanoribbon connecting two ferromagnetic contacts (Kim and Kim, 2008). The low-resistance configuration (a) and the high-resistance configuration (b) of the device correspond to parallel and antiparallel orientations of the magnetic moments of the two ferromagnetic leads, respectively. Arrows denote the magnetic moments of both graphene edges and ferromagnetic leads.

where R^{P} and R^{AP} are the resistances for parallel and antiparallel relative orientations of the magnetic moments of the layers. Magnetoresistive devices with high magnitudes of MR are demanded by the future nanoscale electronics. It has been predicted that a zigzag graphene nanoribbon placed between two ferromagnetic contacts constitutes a magnetoresistive junction with very high values of magnetoresistance ratio (Kim and Kim, 2008). The low-resistance state of the proposed device corresponds to the parallel configuration in which the magnetic moments at graphene edges are coupled ferromagnetically to each other. The ferromagnetic coupling is enforced by the strong interaction with the magnetic moments of ferromagnetic contacts (Fig. 13(a)). In the antiparallel configuration (Fig. 13(b)), the magnetic graphene nanoribbon develops a domain-wall arrangement of edge spins with high resistance. It is worth mentioning that spin-transport measurements in micrometer-scale lateral graphene devices contacted by ferromagnetic electrodes have been carried out experimentally (Hill *et al.*, 2006; Jozsa *et al.*, 2008; Tombros *et al.*, 2007, 2008). However, the magnetoresistance effect observed in these experiments is due to the long spin-diffusion lengths in graphene.

An all-graphene device based on the armchair-zigzag-armchair nanoribbon junction has also been predicted to show magnetoresistance effect (Muñoz-Rojas *et al.*, 2009). In zero applied magnetic field the magnetic coupling between the opposite zigzag edge segments is antiferromagnetic (Fig. 14(a)) and, hence, electric resistance is high due to the gapped electronic state. Sufficiently strong magnetic fields favor the parallel config-

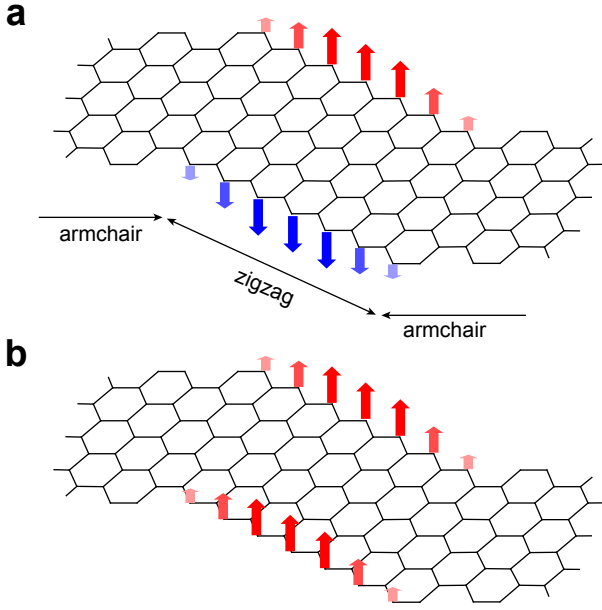


FIG. 14 All-graphene magnetoresistive device proposed in (Muñoz-Rojas *et al.*, 2009). The device represents an armchair-zigzag-armchair nanoribbon junction. The high-resistance antiparallel configuration (a) switches into a low-resistance parallel configuration (b) in a strong enough applied magnetic field.

uration (Fig. 14(b)) which shows a lower resistance due to the spin-polarized edge states crossing the Fermi level (Fig. 9(c)). This ultrasmall device thus acts a magnetic field sensor capable to detect magnetic fields from few hundreds of Gauss to several Tesla at low temperatures.

Epitaxial graphene and the isostructural hexagonal boron nitride (*h*-BN) have been proposed as efficient ultrathin non-magnetic spacers for traditional multilayer magnetoresistive junctions (Karpan *et al.*, 2007, 2008; Yazyev and Pasquarello, 2009). Unlike in the device shown in Fig. 13, mono- or multilayers of graphene or *h*-BN are sandwiched between two ferromagnetic layers. The transport direction is orthogonal to the plane of spacer layers. The key to feasibility of such devices is the fact that the lattice constants of graphene and *h*-BN match closely those of Co and Ni. Moreover, in the case of multilayer graphene the momentum selection criteria allow efficient transport only for the minority-spin channel in the parallel configuration of the device. Very high magnetoresistance ratios have been predicted for multilayer graphene used as a spacer material (Karpan *et al.*, 2007, 2008). Meanwhile, high-quality epitaxial monolayers of both graphene and *h*-BN on ferromagnetic transition metals have been grown experimentally using the chemical vapor deposition techniques (Dedkov *et al.*, 2008a,b; Gruneis and Vyalikh, 2008; Oshima and Nagashima, 1997; Rader *et al.*, 2009; Varykhalov and Rader, 2009; Varykhalov *et al.*, 2008). Successful growth of lower-quality multilayer graphene on polycrystalline Ni substrates has also been reported

(Reina *et al.*, 2009).

Considerable progress has also been achieved in controlled manufacturing of graphene nanostructures. The lithographic patterning allows to produce graphene nanoribbons as narrow as ~ 15 nm (Han *et al.*, 2007). Sub-10-nanometer graphene nanoribbons have been synthesized using a variety of chemical approaches starting from either graphite (Li *et al.*, 2008; Wang *et al.*, 2008b) or carbon nanotubes (Jiao *et al.*, 2009; Kosynkin *et al.*, 2009). Well-ordered edges along a single crystallographic direction of graphene have been produced by means of chemical vapor deposition (Campos-Delgado *et al.*, 2008), annealing by Joule heating (Jia *et al.*, 2009), and anisotropic etching of graphene using metallic nanoparticles (Campos *et al.*, 2009).

C. Magnetic ordering at finite temperatures

It has already been mentioned at the beginning that the Curie temperatures of ferromagnetic materials must be higher than the operation temperature of the device, which is typically supposed to be close to 300 K. When introducing the working principles of the proposed spintronic devices based on graphene edges, temperature-related limitations were not discussed. However, magnetic order in low-dimensional systems is particularly sensible to thermal fluctuations. In particular, the Mermin-Wagner theorem excludes long-range order in one-dimensional magnetic systems (such as the magnetic graphene edges) at any finite temperature (Mermin and Wagner, 1966). The range of magnetic order is limited by the temperature-dependent spin correlation lengths ξ^α ($\alpha = x, y, z$) which define the decay law of the spin correlation

$$\langle \hat{s}_i^\alpha \hat{s}_{i+l}^\alpha \rangle = \langle \hat{s}_i^\alpha \hat{s}_i^\alpha \rangle \exp(-l/\xi^\alpha), \quad (10)$$

where \hat{s}_i^α are the components of magnetic moment unit vector $\hat{\mathbf{s}}_i$ at site i . In principle, the spin correlation length imposes the limitations on the device dimensions. In order to establish this parameter one has to determine the energetics of the spin fluctuations contributing to the breakdown of the ordered ground-state configuration.

The energetics of the transverse and longitudinal spin excitations (Figs. 15(a),(b)) have been explored using density-functional-theory calculations (Yazyev and Katsnelson, 2008). The magnetic correlation parameters in the presence of spin-wave fluctuations, the dominant type of spin disorder in this case, were obtained with the help of one-dimensional Heisenberg model Hamiltonian

$$H = -a \sum_i \hat{\mathbf{s}}_i \hat{\mathbf{s}}_{i+1} - d \sum_i \hat{s}_i^z \hat{s}_{i+1}^z, \quad (11)$$

where the Heisenberg coupling $a = 2\kappa/a_z^2 = 105$ meV corresponds to the spin-wave stiffness $\kappa = 320$ meV \AA^2 calculated from first principles. The estimated small

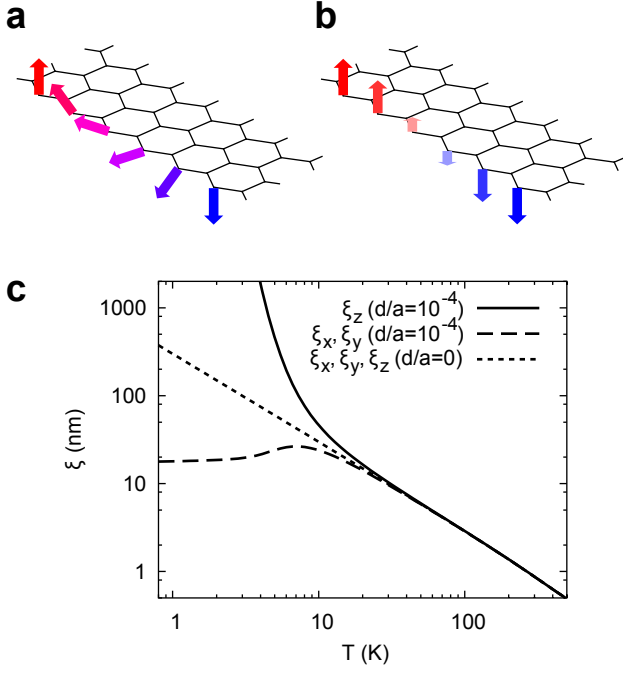


FIG. 15 Schematic representation of the transverse (a) and the longitudinal (b) low-energy spin excitation at zigzag graphene edges. The magnetic moments are shown by arrows. Their directions are represented by orientation and color of the arrows, and the magnitude is shown by their lengths and color intensity. (c) Correlation lengths of magnetization vector components orthogonal (ξ_z) and parallel (ξ_x, ξ_y) to the graphene plane as a function of temperature. Reproduced from (Yazyev and Katsnelson, 2008). Copyright 2008 by the American Physical Society.

anisotropy parameter $d/a \approx 10^{-4}$ originates from the weak spin-orbit interaction in carbon. This simple model Hamiltonian has known analytic solutions (Joyce, 1967). Figure 15(c) shows the spin correlation lengths calculated for our particular case. Above the crossover temperature $T_x \approx 10$ K, weak magnetic anisotropy does not play any role and the spin correlation length $\xi \propto T^{-1}$. However, below T_x the spin correlation length grows exponentially with decreasing temperature. At $T = 300$ K the spin correlation length $\xi \approx 1$ nm.

From a practical point of view, this means that the dimensions of spintronic devices based on the magnetic zigzag edges of graphene and operating at normal temperature conditions are limited to several nanometers. At present, such dimensions are very difficult to achieve, which can be regarded as a pessimistic conclusion. Nevertheless, one has to keep in mind that the spin stiffness predicted for the magnetic graphene edges is still higher than the typical values for traditional magnetic materials. That is, graphene outperforms d -element based magnetic materials, and there is a room for improvement. Achieving control over the magnetic anisotropy d/a could possibly raise the crossover temperature T_x above 300 K and thus significantly extend ξ . Possible approaches for

reaching this goal include chemical functionalization of the edges with heavy-element functional groups or coupling graphene to a substrate.

VI. MAGNETISM IN GRAPHENE AND GRAPHITE

A. Radiation damage and defects in carbon materials

Experimental observations of ferromagnetic ordering in irradiated graphite have already been mentioned in the introductory part of this review. These results are particularly exciting because of the fact that the induced magnetic ordering is stable at room temperature and well above. Let us now try to understand the origin of magnetism in irradiated graphite. The present section covers the cases of both graphene and graphite which has a three-dimensional crystalline lattice composed of weakly coupled graphene layers.

The basic picture of the radiation damage process in carbon materials is relatively simple. Irradiation of graphite with high-energy particles (*e.g.* protons) produces several types of point defects. In carbon materials the defects are created as a result of so-called “knock-on collisions” (Banhart, 1999; Krasheninnikov and Banhart, 2007). This process involves the direct transfer of kinetic energy from the high-energy incident particles to the individual atoms in material’s lattice. If the transferred energy is larger than the displacement threshold T_d , the recoil atom may leave its equilibrium position leading to the formation of a pair of point defects – a *vacancy* defect and an *interstitial*. The structure of the vacancy defect in graphene and graphite is shown in Figure 16(a). In graphene the interstitial defects have a bridge structure (Lehtinen *et al.*, 2003), while in graphite the stable configuration corresponds to a carbon atom trapped between the adjacent graphene layers (Li *et al.*, 2005; Telling *et al.*, 2003) as shown in Figures 16(b). The displacement threshold T_d for carbon atoms in graphitic materials was found to be ~ 20 eV in a number of studies (Crespi *et al.*, 1996; Smith and Luzzi,

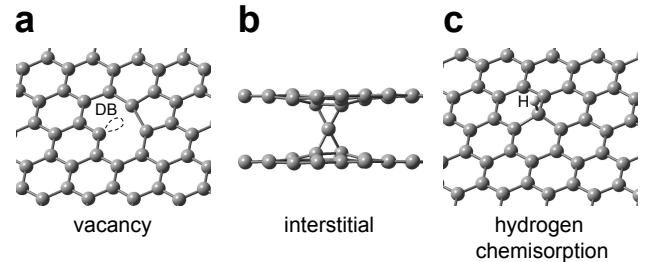


FIG. 16 Atomic structures of primary point defects produced upon irradiating graphite by high-energy protons: (a) single-atom vacancy, (b) interstitial bridging the neighboring graphene layers, and (c) hydrogen chemisorption. The dangling bond (DB) of the reconstructed vacancy defect and the chemisorbed hydrogen atom (H) are labeled.

2001; Yazyev *et al.*, 2007; Zobelli *et al.*, 2007). Creation of defects due to electron stopping, *i.e.* the process involving possible electronic excitations and ionization of individual atoms, is less important in carbon materials since electronic excitations in metals are delocalized and quench instantly (Banhart, 1999; Krashenninnikov and Banhart, 2007).

After slowing down, reactive particles may also produce chemisorption defects. In particular, protons are able to bind to individual carbon atoms in graphene lattice resulting in their rehybridization into the sp^3 -state (Fig. 16(c)). Such defects are referred to as *hydrogen chemisorption* defects. From the point of view of one-orbital models that we use in our review, both vacancy and hydrogen chemisorption defects are equivalent. In both cases a defect removes one p_z -orbital from the π -system of graphene. In the first case, the p_z -orbital is eliminated together with the knocked-out carbon atom. The hydrogen chemisorption does not remove the carbon atom from the crystalline lattice, but once rehybridized the atom is unable to contribute its p_z -orbital to the π -electron system. These two types of defects are further referred to as p_z -vacancies.

The defects described above are the primary defects in the radiation-damage process. More complex defects can be produced at later stages of the process. For instance, single-atom vacancies and interstitials may aggregate producing extended defects. Complexes involving two or more different defects can also be formed upon irradiation. Examples are complexes of hydrogen with vacancies and interstitials (Lehtinen *et al.*, 2004), and intimate Frenkel pairs (Ewels *et al.*, 2003; Yazyev *et al.*, 2007). Radiation damage in graphitic materials may also produce the Stone-Wales defects (Kaxiras and Pandey, 1988; Stone and Wales, 1986).

B. Defect-induced magnetism in graphene

The single atom p_z -vacancies described above have a particularly profound effect on the electronic structure of ideal graphene. Let us consider a periodically repeated supercell of graphene composed of $2N$ ($N_A = N_B = N$) carbon atoms. Elimination of one atom from sublattice A introduces a zero-energy state in the complementary sublattice ($\alpha = N_B$; thus $\eta = 2N_B - ((N_A - 1) + N_B) = 1$). Such zero-energy states extending over large distances are called quasi-localized states since they show a power-law decay (Huang *et al.*, 2009; Pereira *et al.*, 2006). The quasi-localized states have been observed in a large number of scanning tunneling microscopy (STM) studies of graphite as triangular $\sqrt{3} \times \sqrt{3}R30^\circ$ superstructures extending over a few nanometers and localized around point defects (Kelly and Halas, 1998; Mizes and Foster, 1989; Ruffieux *et al.*, 2000). For the single-defect model we have adopted, Lieb's theorem predicts a magnetic moment of $|(N_A - 1) + N_B| = 1\mu_B$ per supercell, that is, the presence of a defect induces ferromagnetic ordering.

This result has been widely confirmed using both first-principles (Duplock *et al.*, 2004; Lehtinen *et al.*, 2004; Yazyev and Helm, 2007) and mean-field Hubbard model (Kumazaki and Hirashima, 2007; Palacios *et al.*, 2008) calculations. Figure 17(a) shows the spin-resolved density-of-states plots for hydrogen chemisorption and vacancy defects obtained using first-principles calculations (Yazyev and Helm, 2007). In the first case, the sharp peak close to the Fermi level corresponds to the quasi-localized state induced by the chemisorbed hydrogen atom. The peak is fully split by exchange and the system is characterized by a magnetic moment of $1\mu_B$ at any defect concentration. The distribution of spin density around the defective site clearly shows a $\sqrt{3} \times \sqrt{3}R30^\circ$ superstructure (Fig. 17(b)). The case of vacancy defect is somewhat more complicated. In addition to the quasi-localized state, there is also a localized non-bonding state due to the presence of a σ -symmetry dangling bond in

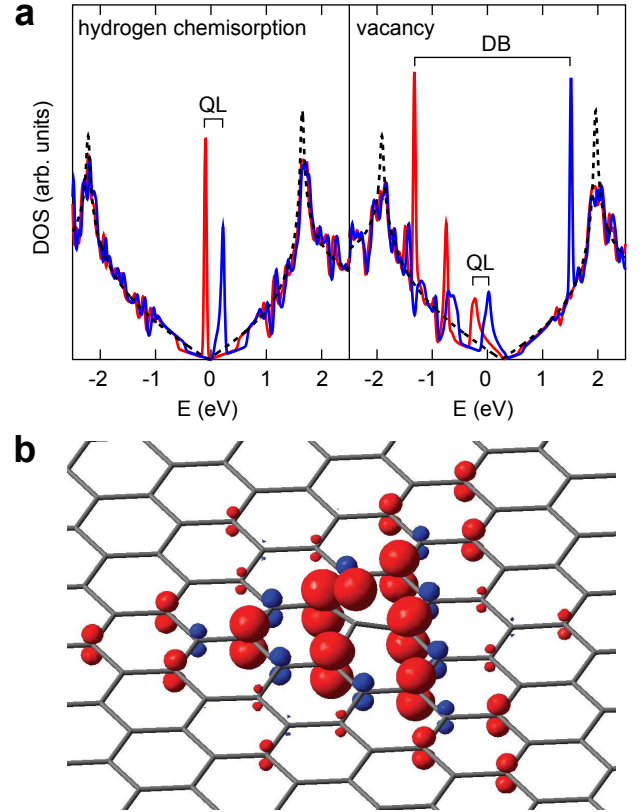


FIG. 17 (a) Spin-resolved density of states (DOS) for the vacancy and the hydrogen chemisorption defect in graphene calculated from first principles. Red and blue curves correspond to the majority and minority spins, respectively. Dashed curve shows the reference density of states of the ideal graphene. Zero energy corresponds to the Fermi level. Exchange-split peaks which correspond to quasi-localized (QL) and dangling-bond (DB) states are labeled. (b) Iso-surface representation of the spin-density distribution at the hydrogen chemisorption defect obtained from first principles. Red and blue surfaces correspond to the majority- and minority-spin densities, respectively.

this defect (Fig. 16(a)). The dangling-bond state shows a very strong exchange splitting and contributes $1\mu_B$ to the total magnetic moment of the defect (Fig. 17(a)). However, the magnetic moment due to the quasi-localized state is partially suppressed in this case due to the self-doping effect related to the structural reconstruction of the vacancy (Yazyev and Helm, 2007). The overall magnetic moment per vacancy defect varies from $1.12\mu_B$ to $1.53\mu_B$ for defect concentrations ranging from 20% to 0.5%.

Magnetic moments due to dangling bonds can also be contributed by other types of defects, *e.g.* the bridge-configuration interstitial defect in graphene (Lehtinen *et al.*, 2003). However, one has to keep in mind that magnetic ordering due to only localized magnetic moments in graphene-based system is improbable at high temperatures. The Ruderman-Kittel-Kasuya-Yoshida interaction is expected to be weak in this case due to the semi-metallic electronic structure of graphene (Brey and Fertig, 2006; Dugaev *et al.*, 2006; Saremi, 2007; Vozmediano *et al.*, 2005). On the other hand, magnetic ordering due to the quasi-localized states can be considered as itinerant magnetism without excluding a possible contribution of dangling-bond magnetic moments to the net magnetic moment of a defective carbon system.

The system with one defect placed in a periodically repeated supercell is only a rough model of disordered graphene for two reasons. First, all defects are located in the same sublattice of the graphene layer. Second, the defects form an ordered periodic superlattice. A more realistic description of disorder can be achieved by constructing models with defects randomly distributed in a large enough supercell (Yazyev, 2008b). Such models allow defects to occupy both sublattices at arbitrary concentrations and eliminate any short-range order in the spatial arrangement of defects. Larger supercells are needed for building the disordered models which makes first-principles calculations impractical. However, such system can still be treated using the mean-field Hubbard model calculations.

Figure 18(a) shows the distribution of spin density in a selected region of a large supercell randomly populated by p_z -vacancies. Defects in different sublattices are shown as black triangles of different orientations. The resulting picture can be explained if one considers the following two arguments. First, from Lieb's theorem the total magnetic per supercell is $M = |N_A - N_B| = |N_B^d - N_A^d|$, where N_A^d and N_B^d are the numbers of defects created in sublattices A and B , respectively. This means that electron spins populating the quasi-localized states in the same sublattice are oriented parallel to each other while the antiparallel arrangement is realized when electron spins populate different sublattices. This conclusion is qualitatively the same as the one we obtained when considering finite graphene nanofragments. Second, quasi-localized states populating complementary sublattices interact with each other

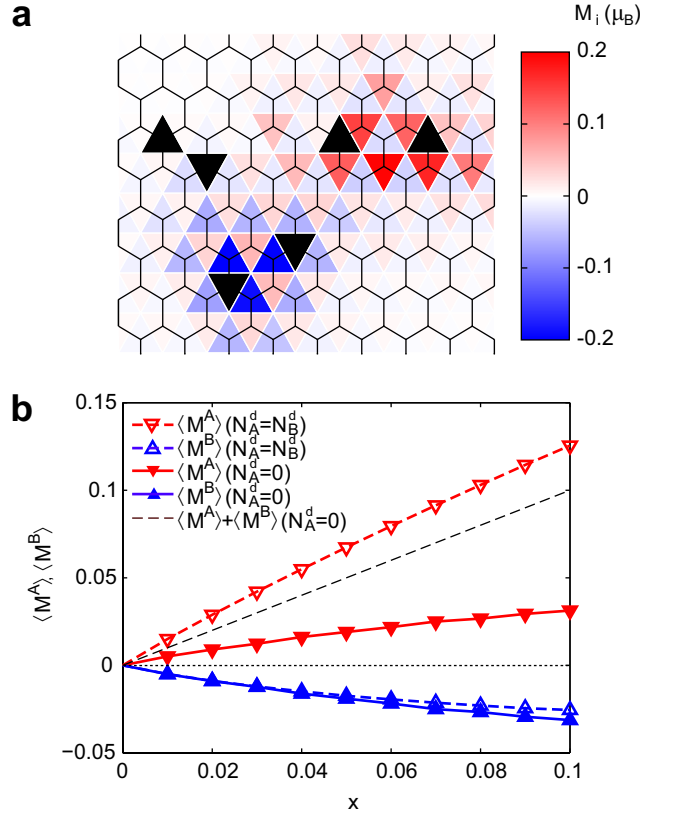


FIG. 18 (a) Distribution of local magnetic moments M_i in a small region a system with random distribution of p_z -vacancies obtained through the mean-field Hubbard model calculations. Positions of defects belonging to sublattices A and B are marked by \blacktriangle and \blacktriangledown , respectively. (b) Average magnetic moments for the atoms in sublattice A ($\nabla, \blacktriangledown$) and sublattice B ($\triangle, \blacktriangle$) as a function of defect concentration x . The defects are either distributed equally between the two sublattices (solid curves/filled symbols) or belong to sublattice B only (dashed curves/empty symbols). Net magnetic moments per carbon atom (dashed line) is shown for the case of defects distributed over sublattice B only.

(Kumazaki and Hirashima, 2007; Palacios *et al.*, 2008). The interaction lifts the degeneracy leading to weakly bonding and anti-bonding states. This provides another mechanism for escaping the instability associated with the presence of low-energy electronic states. The interaction strength between two defects increases with decreasing distance between them. For very short distances, the gain in exchange energy does not compensate for the kinetic energy penalty due to the splitting. This leads to quenching of the defect-induced magnetic moments (Boukhvalov *et al.*, 2008; Yazyev, 2008b). The competition between these effects is demonstrated in Figure 18(a).

More quantitative results are presented in Figure 18(b) which shows the mean magnetic moment $\langle M^A \rangle$ and $\langle M^B \rangle$ per carbon atom in sublattice A and sublattice B as a function of defect concentration x (Yazyev, 2008b).

The resulting values have been averaged over many random placements of defects in the simulation supercell. The plot refers to the situation of defects equally distributed over the two sublattices ($N_A^d = N_B^d$) and to the situation when defects belong to sublattice B only ($N_A^d = 0$). In the first case, the magnetic moments in the two sublattices compensate each other. The overall magnetic ordering is of *antiferromagnetic* character. When defects populate only one sublattice the system exhibits *ferromagnetic* ordering. The net magnetic moment per carbon atom $\langle M \rangle = (\langle M^A \rangle + \langle M^B \rangle)/2 = x/2$ scales linearly with the defect concentration. Both numerical results are in full agreement with Lieb's theorem.

C. Magnetism in graphite and multilayer graphene

Experimental observations of ferromagnetism in irradiated graphite point to the conclusion that sublattices of individual graphene layers in bulk graphite are populated by defects differently: that is, there must be a mechanism which makes the sublattices of graphene inequivalent. Such an intrinsic discriminating mechanism was ascribed to the stacking order of graphite layers in bulk graphite (Yazyev, 2008b). The lowest-energy *ABA* stacking order of individual graphene sheets in graphite breaks the equivalence of the two sublattices as shown in Figure 19(a). In fact, only local *ABA* stacking order is required to discriminate between the two sublattices of the middle sheet. The mechanism can be demonstrated for the case of hydrogen chemisorption defects. First-principles calculations show that the configuration which involves hydrogen chemisorbed on sublattice B is 0.16 eV lower in energy than on sublattice A (see Figs. 19(b) and 19(c)). This energy difference is sufficient to trigger a considerable difference in equilibrium populations of the two sublattices. The energy barrier for the hopping of chemisorbed hydrogen atoms is relatively small (~ 1 eV)

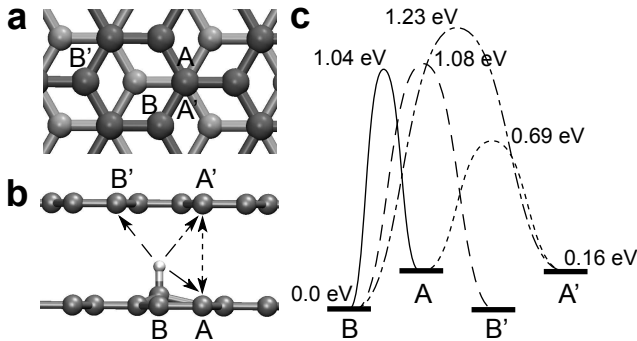


FIG. 19 (a) Inequivalent carbon atoms (A and B) in *ABA* graphite. (b) Possible pathways for the diffusion of chemisorbed hydrogen in graphite. (c) Schematic representation of the potential energy surface for the in-plane diffusion of hydrogen in graphite showing the relative energies for the local minima and transition states. Reproduced from (Yazyev, 2008b). Copyright 2008 by the American Physical Society.

to allow for thermally activated diffusion at mild temperatures.

Similar discriminating mechanisms may also exist for the other types of defects created by irradiation, *e.g.* for vacancies. Cross-sections for momentum transfer during knock-on collisions with high-energy incident particles are likely to be very similar for both A and B carbon atoms in graphite. However, the stacking order may have a strong influence on the recombination of interstitial and vacancy defects close to equilibrium conditions. It was also shown that instantaneous recombination of low-energy recoil atoms in graphite is significantly more probable for atoms in position A (Yazyev *et al.*, 2007). That is, more vacancies in sublattice B are left assuming an equal number of knock-on collisions involving the atoms of both types. These results allow us to conclude that the most probable physical picture of magnetic order in irradiated graphite is *ferrimagnetism*. The magnetic moment induced by defects in sublattice A is larger than the one induced in sublattice B .

It is worth mentioning other possible scenarios for the onset of magnetism in graphene-related materials and nanostructures. It was shown that local negative Gauss curvatures in graphene layers also lead to localized magnetic moments (Park *et al.*, 2003). Coupling between the two graphene layers in a biased graphene bilayer introduces a pair of sharp van Hove singularities close to the Fermi level. It was shown theoretically that in a range of conditions biased bilayer graphene satisfies the Stoner criterion leading to a low-density ferromagnetic phase (Castro *et al.*, 2008).

The question of magnetic ordering in defective graphene and graphite at finite temperatures remains largely unaddressed. Similarly to the one-dimensional system discussed above, an isotropic two-dimensional system cannot develop long-range magnetic ordering at any finite temperature (Mermin and Wagner, 1966). However, the introduction of a small magnetic anisotropy $d/a \sim 10^{-3}$ already leads to very high transition temperatures (Barzola-Quiquia *et al.*, 2007). Weak magnetic coupling between the individual layers in graphite also produces a pronounced effect on the magnetic transition temperature (Pisani *et al.*, 2008).

VII. CONCLUSIONS AND PERSPECTIVES

The review illustrated a rich variety of magnetism scenarios in graphene nanostructures and explained them in terms of simple physical models. Beyond these theoretical considerations the field of carbon-based magnetism faces a number of challenges. The most important problems are related to the experimental side of the field. In particular, the physics of magnetic graphene edges has already attracted a large number of computational and theoretical researchers. However, no direct experimental evidence has been reported at the time this review was written. Further progress in this field will also re-

quire novel manufacturing techniques which would allow control of the edge configuration with truly atomic precision. The area of defect-induced magnetism in graphite demands detailed studies of defects produced upon irradiation and their role in the onset of ferromagnetic ordering. The limits of saturation magnetization and Curie temperature in irradiated graphite have still to be established. On the theory side of this field, an understanding of magnetic phase transitions in graphene materials and nanostructures has to be developed. Other important directions of theoretical research include spin transport and magnetic anisotropy of carbon-based systems.

VIII. ACKNOWLEDGMENTS

I would like to thank J. Fernández-Rossier, Y.-W. Son and D. Strubbe for critical reading of the manuscript. This work was supported by the Swiss National Science Foundation (grant No. PBELP2-123086).

References

- Akola, J., H. P. Heiskanen, and M. Manninen, 2008, *Phys. Rev. B* **77**, 193410.
- Allemand, P.-M., K. C. Khemani, A. Koch, F. Wudl, K. Holczer, S. Donovan, G. Grner, and J. D. Thompson, 1991, *Science* **253**, 301.
- Allinson, G., R. J. Bushby, J.-L. Paillaud, and M. Thornton-Pett, 1995, *J. Chem. Soc., Perkin Trans. 1*, 385.
- Anderson, P. W., 1950, *Phys. Rev.* **79**, 350.
- Awschalom, D. D., and M. E. Flatte, 2007, *Nature Phys.* **3**, 153.
- Banhart, F., 1999, *Rep. Prog. Phys.* **62**, 1181.
- Barone, V., O. Hod, and G. E. Scuseria, 2006, *Nano Lett.* **6**, 2748.
- Barzola-Quiquia, J., P. Esquinazi, M. Rothermel, D. Spemann, T. Butz, and N. Garcia, 2007, *Phys. Rev. B* **76**, 161403.
- Barzola-Quiquia, J., R. Höhne, M. Rothermel, A. Setzer, P. Esquinazi, and V. Heera, 2008, *Eur. Phys. J. B* **61**, 127.
- Boukhvalov, D. W., M. I. Katsnelson, and A. I. Lichtenstein, 2008, *Phys. Rev. B* **77**, 035427.
- Brey, L., and H. A. Fertig, 2006, *Phys. Rev. B* **73**, 235411.
- Brey, L., H. A. Fertig, and S. Das Sarma, 2007, *Phys. Rev. Lett.* **99**, 116802.
- Campos, L. C., V. R. Manfrinato, J. D. Sanchez-Yamagishi, J. Kong, and P. Jarillo-Herrero, 2009, *Nano Lett.* **9**, 2600.
- Campos-Delgado, J., J. M. Romo-Herrera, X. Jia, D. A. Cullen, H. Muramatsu, Y. A. Kim, T. Hayashi, Z. Ren, D. J. Smith, Y. Okuno, T. Ohba, H. Kanoh, *et al.*, 2008, *Nano Lett.* **8**, 2773.
- Cantele, G., Y.-S. Lee, D. Ninno, and N. Marzari, 2009, *Nano Lett.* **9**, 3425.
- Castro, E. V., N. M. R. Peres, T. Stauber, and N. A. P. Silva, 2008, *Phys. Rev. Lett.* **100**, 186803.
- Castro Neto, A. H., F. Guinea, N. M. R. Peres, K. S. Novoselov, and A. K. Geim, 2009, *Rev. Mod. Phys.* **81**, 109.
- Červenka, J., M. I. Katsnelson, and C. F. J. Flipse, 2009, *Nature Phys.* **5**, 840.
- Chappert, C., A. Fert, and F. N. Van Dau, 2007, *Nature Mater.* **6**, 813.
- Clar, E., 1972, *The Aromatic Sextet* (Wiley, London).
- Clar, E., and C. C. Mackay, 1972, *Tetrahedron* **28**, 6041.
- Crespi, V. H., N. G. Chopra, M. L. Cohen, A. Zettl, and S. G. Louie, 1996, *Phys. Rev. B* **54**, 5927.
- Dedkov, Y. S., M. Fonin, and C. Laubschat, 2008a, *Appl. Phys. Lett.* **92**, 052506.
- Dedkov, Y. S., M. Fonin, U. Rudiger, and C. Laubschat, 2008b, *Appl. Phys. Lett.* **93**, 022509.
- Dugaev, V. K., V. I. Litvinov, and J. Barnas, 2006, *Phys. Rev. B* **74**, 224438.
- Duplock, E. J., M. Scheffler, and P. J. D. Lindan, 2004, *Phys. Rev. Lett.* **92**, 225502.
- Edwards, D. M., and M. I. Katsnelson, 2006, *J. Phys.: Condens. Matter* **18**, 7209.
- Esquinazi, P., A. Setzer, R. Höhne, C. Semmelhack, Y. Kopelevich, D. Spemann, T. Butz, B. Kohlstrunk, and M. Lösche, 2002, *Phys. Rev. B* **66**, 024429.
- Esquinazi, P., D. Spemann, R. Höhne, A. Setzer, K.-H. Han, and T. Butz, 2003, *Phys. Rev. Lett.* **91**, 227201.
- Ewels, C. P., R. H. Telling, A. A. El-Barbary, M. I. Heggie, and P. R. Briddon, 2003, *Phys. Rev. Lett.* **91**, 025505.
- Ezawa, M., 2006, *Phys. Rev. B* **73**, 045432.
- Ezawa, M., 2007, *Phys. Rev. B* **76**, 245415.
- Ezawa, M., 2008, *Phys. Rev. B* **77**, 155411.
- Ezawa, M., 2009a, *Phys. Rev. B* **79**(24), 241407.
- Ezawa, M., 2009b, *Eur. Phys. J. B* **67**, 543.
- Fajtlowicz, S., P. E. John, and H. Sachs, 2005, *Croat. Chem. Acta* **78**, 195.
- Feldner, H., A. Honecker, D. Cabra, S. Wessel, Z. Y. Meng, and F. F. Assaad, 2009, arXiv:0910.5360 .
- Fernández-Rossier, J., 2008, *Phys. Rev. B* **77**, 075430.
- Fernández-Rossier, J., and J. J. Palacios, 2007, *Phys. Rev. Lett.* **99**, 177204.
- Fert, A., 2008, *Rev. Mod. Phys.* **80**, 1517.
- Fischer, J., B. Trauzettel, and D. Loss, 2009, *Phys. Rev. B* **80**, 155401.
- Fujita, M., K. Wakabayashi, K. Nakada, and K. Kusakabe, 1996, *J. Phys. Soc. Jpn.* **65**, 1920.
- Geim, A. K., and K. S. Novoselov, 2007, *Nature Mater.* **6**, 183.
- Gruneis, A., and D. V. Vyalikh, 2008, *Phys. Rev. B* **77**, 193401.
- Gunlycke, D., D. A. Areshkin, J. Li, J. W. Mintmire, and C. T. White, 2007, *Nano Lett.* **7**, 3608.
- Han, M. Y., B. Ozyilmaz, Y. Zhang, and P. Kim, 2007, *Phys. Rev. Lett.* **98**, 206805.
- Heiliger, C., P. Zahn, and I. Mertig, 2006, *Materials Today* **9**, 46.
- Hill, E. W., A. K. Geim, K. Novoselov, F. Schedin, and P. Blake, 2006, *IEEE Trans. Magn.* **42**, 2694.
- Huang, W.-M., J.-M. Tang, and H.-H. Lin, 2009, *Phys. Rev. B* **80**, 121404.
- Inoue, J., K. Fukui, T. Kubo, S. Nakazawa, K. Sato, D. Shiomi, Y. Morita, K. Yamamoto, T. Takui, and K. Nakasuji, 2001, *J. Am. Chem. Soc.* **123**, 12702.
- Jia, X., M. Hofmann, V. Meunier, B. G. Sumpter, J. Campos-Delgado, J. M. Romo-Herrera, H. Son, Y.-P. Hsieh, A. Reina, J. Kong, M. Terrones, and M. S. Dresselhaus, 2009, *Science* **323**, 1701.
- Jiao, L., L. Zhang, X. Wang, G. Diankov, and H. Dai, 2009, *Nature* **458**, 877.
- Joyce, G. S., 1967, *Phys. Rev. Lett.* **19**, 581.

- Jozsa, C., M. Popinciuc, N. Tombros, H. T. Jonkman, and B. J. van Wees, 2008, *Phys. Rev. Lett.* **100**, 236603.
- Jung, J., and A. H. MacDonald, 2009, *Phys. Rev. B* **79**, 235433.
- Jung, J., T. Pereg-Barnea, and A. H. MacDonald, 2009, *Phys. Rev. Lett.* **102**, 227205.
- Karpan, V. M., G. Giovannetti, P. A. Khomyakov, M. Talanana, A. A. Starikov, M. Zwierzycki, J. van den Brink, G. Brocks, and P. J. Kelly, 2007, *Phys. Rev. Lett.* **99**, 176602.
- Karpan, V. M., P. A. Khomyakov, A. A. Starikov, G. Giovannetti, M. Zwierzycki, M. Talanana, G. Brocks, J. van den Brink, and P. J. Kelly, 2008, *Phys. Rev. B* **78**, 195419.
- Katsnelson, M. I., 2007, *Materials Today* **10**, 20.
- Kaxiras, E., and K. C. Pandey, 1988, *Phys. Rev. Lett.* **61**, 2693.
- Kelly, K. F., and N. J. Halas, 1998, *Surf. Sci.* **416**, L1085.
- Kim, W. Y., and K. S. Kim, 2008, *Nature Nanotechnol.* **3**, 408.
- Kobayashi, Y., K.-i. Fukui, T. Enoki, and K. Kusakabe, 2006, *Phys. Rev. B* **73**, 125415.
- Kobayashi, Y., K.-i. Fukui, T. Enoki, K. Kusakabe, and Y. Kaburagi, 2005, *Phys. Rev. B* **71**, 193406.
- Koch, W., and M. C. Holthausen, 2002, *A Chemist's Guide to Density Functional Theory* (Wiley-VCH, Weinheim).
- Kopelevich, Y., P. Esquinazi, J. H. S. Torres, and S. Moehlecke, 2000, *J. Low Temp. Phys.* **119**, 691.
- Kosynkin, D. V., A. L. Higginbotham, A. Sinitskii, J. R. Lomeda, A. Dimiev, B. K. Price, and J. M. Tour, 2009, *Nature* **458**, 872.
- Kramers, H. A., 1934, *Physica* **1**, 182.
- Krasheninnikov, A. V., and F. Banhart, 2007, *Nature Mater.* **6**, 723.
- Kumazaki, H., and D. S. Hirashima, 2007, *J. Phys. Soc. Jpn.* **76**, 064713.
- Kuroda, S., and H. Shirakawa, 1987, *Phys. Rev. B* **35**, 9380.
- Lakshmi, S., S. Roche, and G. Cuniberti, 2009, *Phys. Rev. B* **80**, 193404.
- Lehtinen, P., A. S. Foster, A. Ayuela, A. Krasheninnikov, K. Nordlund, and R. M. Nieminen, 2003, *Phys. Rev. Lett.* **91**, 017202.
- Lehtinen, P. O., A. S. Foster, Y. Ma, A. Krasheninnikov, and R. M. Nieminen, 2004, *Phys. Rev. Lett.* **93**, 187202.
- Li, L., S. Reich, and J. Robertson, 2005, *Phys. Rev. B* **72**, 184109.
- Li, X., X. Wang, L. Zhang, S. Lee, and H. Dai, 2008, *Science* **319**, 1229.
- Lieb, E. H., 1989, *Phys. Rev. Lett.* **62**, 1201.
- Makarova, T., and F. Palacio, 2006, *Carbon Based Magnetism: An Overview of the Magnetism of Metal Free Carbon-based Compounds and Materials* (Elsevier, Amsterdam).
- Makarova, T. L., B. Sundqvist, R. Höhne, P. Esquinazi, Y. Kopelevich, P. Scharff, V. Davydov, L. S. Kashevarova, and A. V. Rakhmanina, 2006, *Nature (London)* **440**, 707.
- Makarova, T. L., B. Sundqvist, R. Höhne, P. Esquinazi, Y. Kopelevich, P. Scharff, V. A. Davydov, L. S. Kashevarova, and A. V. Rakhmanina, 2001, *Nature (London)* **413**, 716.
- Martin, R. M., 2004, *Electronic Structure: Basic Theory and Practical Methods* (Cambridge University Press, Cambridge).
- Marx, D., and J. Hutter, 2009, *Ab Initio Molecular Dynamics: Basic Theory And Advanced Methods* (Cambridge University Press, Cambridge).
- Matte, H. S. S. R., K. S. Subrahmanyam, and C. N. R. Rao, 2009, *J. Phys. Chem. C* **113**, 9982.
- Mermin, N. D., and H. Wagner, 1966, *Phys. Rev. Lett.* **17**, 1133.
- Mizes, H. A., and J. S. Foster, 1989, *Science* **244**, 559.
- Mohn, P., 2003, *Magnetism in the Solid State: An Introduction*, Springer Series in Solid-State Sciences (Springer-Verlag, Berlin).
- Muñoz-Rojas, F., J. Fernández-Rossier, and J. J. Palacios, 2009, *Phys. Rev. Lett.* **102**, 136810.
- Nakada, K., M. Fujita, G. Dresselhaus, and M. S. Dresselhaus, 1996, *Phys. Rev. B* **54**, 17954.
- Novoselov, K. S., A. K. Geim, S. V. Morozov, D. Jiang, Y. Zhang, S. V. Dubonos, I. V. Grigorieva, and A. A. Firsov, 2004, *Science* **306**, 666.
- Ohldag, H., T. Tylliszczak, R. Höhne, D. Spemann, P. Esquinazi, M. Ungureanu, and T. Butz, 2007, *Phys. Rev. Lett.* **98**, 187204.
- Oshima, C., and A. Nagashima, 1997, *J. Phys.: Condens. Matter* **9**, 1.
- Palacios, J. J., J. Fernández-Rossier, and L. Brey, 2008, *Phys. Rev. B* **77**, 195428.
- Park, J., H. Yang, K. S. Park, and E.-K. Lee, 2009, *J. Chem. Phys.* **130**, 214103.
- Park, N., M. Yoon, S. Berber, J. Ihm, E. Osawa, and D. Tománek, 2003, *Phys. Rev. Lett.* **91**, 237204.
- Pereira, V. M., F. Guinea, J. M. B. Lopes dos Santos, N. M. R. Peres, and A. H. Castro Neto, 2006, *Phys. Rev. Lett.* **96**, 036801.
- Peres, N. M. R., A. H. Castro Neto, and F. Guinea, 2006, *Phys. Rev. B* **73**, 195411.
- Pisani, L., J. A. Chan, B. Montanari, and N. M. Harrison, 2007, *Phys. Rev. B* **75**, 064418.
- Pisani, L., B. Montanari, and N. M. Harrison, 2008, *New J. Phys.* **10**, 033002.
- Rader, O., A. Varykhalov, J. Sanchez-Barriga, D. Marchenko, A. Rybkin, and A. M. Shikin, 2009, *Phys. Rev. Lett.* **102**, 057602.
- Reina, A., X. Jia, J. Ho, D. Nezich, H. Son, V. Bulovic, M. S. Dresselhaus, and J. Kong, 2009, *Nano Lett.* **9**, 30.
- Rocha, A. R., T. B. Martins, A. Fazzio, and A. J. R. da Silva, 2009, arXiv:0907.5027.
- Ruffieux, P., O. Gröning, P. Schwaller, L. Schlapbach, and P. Gröning, 2000, *Phys. Rev. Lett.* **84**, 4910.
- Saremi, S., 2007, *Phys. Rev. B* **76**, 184430.
- Sawada, K., F. Ishii, M. Saito, S. Okada, and T. Kawai, 2009, *Nano Lett.* **9**, 269.
- Smith, B. W., and D. E. Luzzi, 2001, *J. Appl. Phys.* **90**, 3509.
- Son, Y.-W., M. L. Cohen, and S. G. Louie, 2006a, *Phys. Rev. Lett.* **97**, 216803.
- Son, Y.-W., M. L. Cohen, and S. G. Louie, 2006b, *Nature (London)* **444**, 347.
- Sorella, S., and E. Tosatti, 1992, *Europhys. Lett.* **19**, 699.
- Stone, A. J., and D. J. Wales, 1986, *Chem. Phys. Lett.* **128**, 501.
- Szabo, A., and N. S. Ostlund, 1982, *Modern Quantum Chemistry: Introduction to Advanced Electronic Structure Theory* (Macmillan, New York).
- Takahashi, M., P. Turek, Y. Nakazawa, M. Tamura, K. Nozawa, D. Shiomi, M. Ishikawa, and M. Kinoshita, 1991, *Phys. Rev. Lett.* **67**, 746.
- Tamura, M., Y. Nakazawa, D. Shiomi, K. Nozawa, Y. Hosokoshi, M. Ishikawa, M. Takahashi, and M. Ki-

- noshita, 1991, Chem. Phys. Lett. **186**, 401.
- Telling, R. H., C. P. Ewels, A. A. El-Barbary, and M. I. Heggie, 2003, Nature Mater. **2**, 333.
- Thomann, H., L. R. Dalton, M. Grabowski, and T. C. Clarke, 1985, Phys. Rev. B **31**, 3141.
- Tombros, N., C. Jozsa, M. Popinciuc, H. T. Jonkman, and B. J. van Wees, 2007, Nature **448**, 571.
- Tombros, N., S. Tanabe, A. Veligura, C. Jozsa, M. Popinciuc, H. T. Jonkman, and B. J. van Wees, 2008, Phys. Rev. Lett. **101**, 046601.
- Trauzettel, B., D. V. Bulaev, D. Loss, and G. Burkard, 2007, Nature Phys. **3**, 192.
- Varykhalov, A., and O. Rader, 2009, Phys. Rev. B **80**, 035437.
- Varykhalov, A., J. Sanchez-Barriga, A. M. Shikin, C. Biswas, E. Vescovo, A. Rybkin, D. Marchenko, and O. Rader, 2008, Phys. Rev. Lett. **101**, 157601.
- Vozmediano, M. A. H., M. P. Lopez-Sancho, T. Stauber, and F. Guinea, 2005, Phys. Rev. B **72**, 155121.
- Wang, W. L., S. Meng, and E. Kaxiras, 2008a, Nano Lett. **8**, 241.
- Wang, W. L., O. V. Yazyev, S. Meng, and E. Kaxiras, 2009a, Phys. Rev. Lett. **102**, 157201.
- Wang, X., Y. Ouyang, X. Li, H. Wang, J. Guo, and H. Dai, 2008b, Phys. Rev. Lett. **100**, 206803.
- Wang, Y., Y. Huang, Y. Song, X. Zhang, Y. Ma, J. Liang, and Y. Chen, 2009b, Nano Lett. **9**, 220.
- Wimmer, M., I. Adagideli, S. Berber, D. Tomanek, and K. Richter, 2008, Phys. Rev. Lett. **100**, 177207.
- Wolf, S. A., D. D. Awschalom, R. A. Buhrman, J. M. Daughton, S. von Molnar, M. L. Roukes, A. Y. Chtchelkanova, and D. M. Treger, 2001, Science **294**, 1488.
- Wu, J., W. Pisula, and K. Mullen, 2007, Chem. Rev. **107**, 718.
- Xia, H., W. Li, Y. Song, X. Yang, X. Liu, M. Zhao, Y. Xia, C. Song, T.-W. Wang, D. Zhu, J. Gong, and Z. Zhu, 2008, Adv. Mater. **20**, 4679.
- Yazyev, O. V., 2008a, Nano Lett. **8**, 1011.
- Yazyev, O. V., 2008b, Phys. Rev. Lett. **101**, 037203.
- Yazyev, O. V., and L. Helm, 2007, Phys. Rev. B **75**, 125408.
- Yazyev, O. V., and M. I. Katsnelson, 2008, Phys. Rev. Lett. **100**, 047209.
- Yazyev, O. V., and A. Pasquarello, 2009, Phys. Rev. B **80**, 035408.
- Yazyev, O. V., I. Tavernelli, L. Helm, and U. Rothlisberger, 2005, Phys. Rev. B **71**, 115110.
- Yazyev, O. V., I. Tavernelli, U. Rothlisberger, and L. Helm, 2007, Phys. Rev. B **75**, 115418.
- Yazyev, O. V., W. L. Wang, S. Meng, and E. Kaxiras, 2008, Nano Lett. **8**, 766.
- Zobelli, A., A. Gloter, C. P. Ewels, G. Seifert, and C. Colliex, 2007, Phys. Rev. B **75**, 245402.